Applied Thermal Engineering 124 (2017) 1123–1133

Contents lists available at ScienceDirect

Applied Thermal Engineering

journal homepage: www.elsevier.com/locate/apthermeng

Research Paper

Melting dynamics of a phase change material (PCM) with dispersed metallic nanoparticles using transport coefficients from empirical and mean field models

Santiago Madruga *, Gonzalo S. Mischlich

Department of Applied Mathematics to Aerospace Engineering, School of Aeronautics and Aerospace Engineering, Universidad Politécnica de Madrid (UPM), Plaza Cardenal Cisneros 3, 28040 Madrid, Spain

ARTICLE INFO

Article history:
Received 28 September 2016
Revised 26 May 2017
Accepted 17 June 2017
Available online 20 June 2017

Keywords:
Nanofluid
PCM
Convection
Nanoparticles

ABSTRACT

We study the melting process of *n*-octadecane with dispersed Al_2O_3 nanoparticles in a semicircle. The effective transport coefficients of the resulting nanofluid are modeled with (i) mean field models due to Maxwell-Garnett for the conductivity and Brinkmann for viscosity, and (ii) an empirical model based on a least square fit to experimental data due to Corcione (2011). In both cases, we consider a uniform nanoparticle distribution in the liquid and solid phases and incorporate as well the change of conductivity in the latter phase. We carry out simulations with the transport coefficients predicted by both models and find that Maxwell & Brinkmann overestimates heat transfer rates compared to the empirical fit for most of the ranges of nanoparticle concentration, size, and temperature. However, the proper selection of nanoparticles attending to their size and temperature can lead to enhanced heat transfer, even beyond of mean field model predictions. We show how the effective Prandtl number is the single most important parameter that determines the dynamics and duration of the melting process, and how predictions of our simulations agree with recent experiments (Ho and Gao, 2009).

1. Introduction

Phase Change Materials (PCM) exploit the latent heat of the solid/liquid phase change to store a large amount of heat energy during melting or release it to the environment during solidification, hardly changing the temperature during the process. This stability with respect to temperature changes and thermal storage capacity is key in many industrial applications of these materials such as electronic cooling, air conditioning in buildings, waste heat recovery or to compensate the time offset between energy production and consumption in solar power plants.

A major issue in thermal regulation with PCMs is the low conductivity typical of these materials, which leads to long times during the heat storage and release phases. Many solutions have been proposed to remedy this shortcoming by introducing high conductivity metals within the PCM, often as metallic fins, or embedding the PCM in a metallic porous foam [3,22]. Another promising solution which holds high potential to increase the heat transfer rate, without adding complexity to the device, is the dispersion in the PCM of metallic particles of sizes in the range of tens of nanometers at small volume fractions, forming the named Nano-enhanced PCM (NePCM). In contrast to micrometer size particles, they do not sediment, clog or produce considerable pressure drops [18].

Heat transfer performance and dynamics of the resulting nanofluid (base fluid plus nanoparticles) depends critically on its effective thermal conductivity and viscosity. Because of that, a large number of experiments have been carried out to measure these values in aqueous and non-aqueous fluids, specially on Cu, Al_2O_3, CuO and TiO_2 nanoparticles [10,40].

In addition, sophisticated theoretical models have been developed to predict the conductivity for a given combination liquid/nanoparticle at rest (Maxwell-Garnett, Hamilton-Crosser, Bruggeman, Jeffrey, Davis, etc.) and viscosity (Einstein, Brinkmann, Batchelor, etc). These models tend to underestimate the value of these transport coefficients as a function of nanoparticle concentrations, and they are not completely satisfactory even when micro-mixing effects due to Brownian motion are included [27].

A different approach to determining the effective transport coefficients is to fit available experimental data with a least square regression. Corcione [12] uses experimental data of suspensions of a large set of metallic nanoparticles in water and ethylene glycol at volume fractions ranging from 0.002 to 0.09 and temperatures

* Corresponding author.
E-mail address: santiago.madruga@upm.es (S. Madruga).

http://dx.doi.org/10.1016/j.applthermaleng.2017.06.097
1359-4311/

from 294 K to 324 K to predict the thermal conductivity. Suspensions in water, ethanol, ethylene glycol and propylene at volume fractions from 0.0001 to 0.071 and temperatures from 293 K to 333 K are used to predict the viscosity. Although given the complexity of base fluid and nanoparticles interactions no current theories or single correlations can predict the broad spectrum of experimental data, predictions from this fit are better than proposed theoretical models at a wide range of volume fractions.

The potential of metallic nanoparticles in heat transfer applications with PCMs has prompted the study of these systems during most of the last decade. Experiments with Cu nanoparticles of size 25 nm at 1 wt% on paraffin on a conductive state have found an enhanced melting/solidification rates about 33% [43]. Ho and Gao [19] measured the viscosity and conductivity of Al_2O_3 nanoparticles in *n*-octadecane and found the relative increase of effective viscosity was larger than that of thermal conductivity, casting doubt on the heat transfer enhancement of this nanofluid. Motahar et al. [30] studied as well the thermal conductivity and viscosity on *n*-octadecane but with mesoporous silica particles of size about 300 nm at 1 wt.% and 5 wt.% showing a boost of non-Newtonian viscosity of 60% and conductivity only 5%. Jesumathy et al. [23] studied paraffin wax with 40 nm size CuO particles at 2, 5 and 10 wt.% in a complex annular heat storage system with a heat transfer fluid flowing through the inner cylinder and found a reduced melting time of 13, 21 and 35% for these volume fractions accompanied by a substantial decrease of latent heat. Reduction of subcooling in water with Al_2O_3 nanoparticles has been as well reported [42]. A recent experimental work [31] on the thermal behavior of a paraffin wax with dispersed alumina nanoparticles shows that not only volume fractions and conductivity of nanoparticles determine the heat transfer capability of this nano-enhanced PCM, but as well temperature and diameters of nanoparticles. The overall interplay between conduction, where metallic nanoparticles always speed up the heat transfer, and convection, where viscosity and conductivity are competitive, determine the final heat transfer performance of nano-enhanced PCMs.

Simulations of nanoparticle enhanced PCMs have been carried out using a modified Maxwell-Garnett model for conductivity and Brinkmann for viscosity in water with copper nanoparticles in a rectangle subjected to lateral heating [25] or within an enclosure with lateral wavy surfaces [1]. Other materials like RT27 with copper nanoparticles have been used inside a spherical container filled up to 85% of capacity to simulate a void [20], paraffin wax with copper nanoparticles in a square geometry [32], or *n*-octadecane with CuO nanoparticles within annular, square and cylinder geometries with a finite element method by Dhaidan et al. [16,14,15].

Variations from Maxwell-Garnett and Brinkmann models have been carried out replacing Brinkmann's model for viscosity. For instance, Kashani et al. [24] simulate copper nanoparticles dispersed in *n*-hexadecane in a rectangular geometry subjected to lateral heating using Corcione's empirical fit for viscosity. As well Arasu and Mujumdar [5] uses an exponential model for the viscosity to simulate the melting of a paraffin wax with Al_2O_3 nanoparticles in a square geometry subjected to lateral heating, and find a faster melting rate for small volume fractions of the nanoparticles.

The spherical geometry is specially interesting in micro-encapsulated phase change materials, where the PCMs are encapsulated in a polymeric spherical shell. It has been thoroughly studied analytically, numerically and experimentally, both in melting and solidification processes [11,26,34,21]. However, to account for the thermal expansion of the PCM, due to the difference in densities between the liquid and solid phases, it is usual to leave a space in the container generating unfilled spherical geometries [6,33]. For this same reason, voids appear in all encapsulated phase change materials. For the case of spherical and cylindrical geometries, the voids break the mid-plane symmetry and importantly affect the heat transfer complicating the thermal boundary conditions, since the upper free surface is open to air and the curved part is in contact with the enclosure. In this work, a bidimensional geometry in the form of a semicircle will be used, with a conductive curved part and adiabatic upper surface like happens in voids within spherical or cylindrical containers.

Most of the simulations on nanoparticle enhanced PCMs are based on commercial CFD software and a lesser amount of in-house codes. However, Open Source code is an attractive long term option to compare and validate results on involved phase change simulations. From these considerations, we will use the Open Source code OpenFoam to carry out the simulations presented in this work.

From the whole previous discussion, we aim at studying the melting of *n*-octadecane in half a disk with dispersed Al_2O_3 nanoparticles of sizes 25 nm, 50 nm and 100 nm . We follow two models to calculate the transport coefficients: (i) the mean field models due to Maxwell-Garnett for conductivity and Brinkmann for viscosity, (ii) an empirical fit to experimental data due to Corcione. To carry out the numerical simulations, we use the Open Source code OpenFoam based on the finite volume method.

In Section 2 we present the equations of the model, with a discussion of the models selected for the effective conductivity and viscosity. The next Section 3 explains the algorithms we follow to solve the equations and validate our code with experimental and numerical results available in the literature of PCMs. The results of our simulations are presented in Section 4, where we observe how the most frequently used Maxwell-Garnett and Brinkmann models underestimate the duration of the melting process compared to use transport coefficients derived from an empirical fit in most of the parameter space. We show how the effective Prandtl number can be used to estimate the heat transfer performance of nanoparticle/liquified PCM combinations. This section includes as well a comparison with a simpler conductive phase change process and the effect of volume fraction and size of nanoparticles in the melting process. Finally, conclusions of our work are provided in Section 5.

2. Basic equations and modeling

The geometry consists of a semicircle of radius 2 cm (c.f. Fig. 1). The internal area (6.3 cm^2) is within the order of other simulations

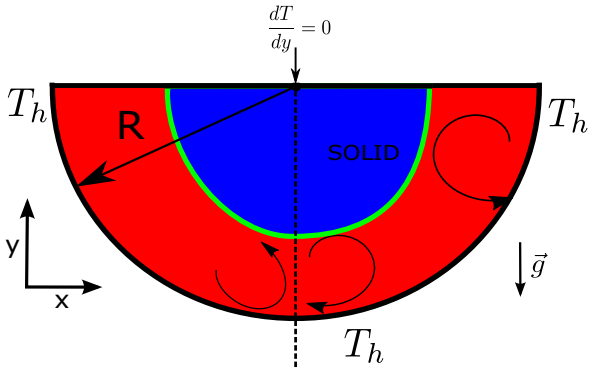

Fig. 1. Sketch of the computational domain. The inner semicircle represents the solid phase of the PCM, and the region between it and the domain boundary the liquid phase. The curved boundary is subjected to a constant temperature T_h, and the upper flat part of the boundary is adiabatic. Idealized convective cells appear as long arrows.

Table 1
Thermophysical properties of *n*-octadecane (subscript *s* for the solid state and *l* for the liquid state) and Al_2O_3 nanoparticles (subscript *np*). Values for the solid and liquid states are listed for the cases distinguished in the equations.

ρ (kg m^{-3}) Ho and Gao [19]	776
μ (N s m^{-2}) Ho and Gao [19]	$3.6 \cdot 10^{-3}$
$c_s \vert c_l$ (J kg^{-1} K^{-1}) Alawadhi [4]	1934|2196
$\lambda_s \vert \lambda_l$ (W m^{-1} K^{-1}) Ho and Gao [19]	0.358|0.13
$T_s \vert T_l$ (K) Ho and Gao [19]	298.25|299.65
L (J Kg^{-1}) Ho and Gao [19]	$243.5 \cdot 10^3$
α (K^{-1}) Dhaidan et al. [15]	$9.1 \cdot 10^{-4}$
λ_{np} (W m^{-1} K^{-1}) Lin and Violi [28]	46
c_{np} (J kg^{-1} K^{-1}) Lin and Violi [28]	850
ρ_{np} (kg m^{-3}) Lin and Violi [28]	3900
α_{np} (K^{-1}) Lin and Violi [28]	$1.67 \cdot 10^{-5}$

on PCMs [34,13,6]. The curved part of the domain is conductive and held at a constant temperature $T_h = 100\ ^\circ$C, greater than the melting temperature of the *n*-octadecane ($T_l = 26.1\ ^\circ$C), which is initially in the solid state ($T_i = 25\ ^\circ$C). The flat part of the boundary is adiabatic, behaving like a free surface without heat exchange with the surroundings. The thermophysical properties of *n*-octadecane are listed in Table 1,

We consider the flow laminar, two-dimensional, and incompressible. For simplicity, viscous dissipation is neglected, nanofluid considered a single phase, and nanoparticles and surrounding PCM are supposed to be in local thermal equilibrium. The physical properties are supposed to be constant within the range of temperatures studied, except the density in the buoyancy term, following the Boussinesq approximation. The origin of a Cartesian frame is placed in the center of the circular section of the domain. The governing equations expressing the balance of momentum and energy, together with the continuity equation, read

$$\rho_{nf}\left[\frac{\partial \mathbf{u}}{\partial t} + (\mathbf{u}\cdot\nabla)\mathbf{u}\right] = -\nabla p + \mu_{eff}\nabla^2\mathbf{u} - g\left[\rho_{nf} - (\rho\alpha)_{nf}(T - T_{ref})\right]\mathbf{e_y} - \frac{C(1-f_l)^2}{\delta + f_l^3}\mathbf{u}, \tag{1}$$

$$\left[\frac{\partial H}{\partial t} + \nabla\cdot(\mathbf{u}H)\right] = \nabla\cdot(\lambda_{eff}\nabla T), \tag{2}$$

and

$$\nabla\cdot\mathbf{u} = 0, \tag{3}$$

respectively. Where $\nabla = (\partial_x, \partial_y)$ and ∂_t are the spatial and temporal operators, T is the volume-averaged temperature of a representative *elementary volume* that can contain solidified nanofluid, liquid nanofluid or a mixture of both phases in local thermal equilibrium; $\mathbf{u} = (u, v)$ is the velocity, being u and v the horizontal and vertical components; μ_{eff} is the dynamic effective viscosity of the nanofluid, p is the pressure, g is the magnitude of the gravity acceleration in the buoyancy term responsible of thermal convective motions, $\mathbf{e_y}$ a unit vector pointing in the vertical direction upwards, T_{ref} is a reference temperature where physical properties are given. The density of the nanofluid ρ_{nf} and the thermal expansion coefficient α are averaged by the volume fraction of nanoparticles ϕ according to $\rho_{nf} = (1-\phi)\rho_l + \phi\rho_{np}$ and $(\rho\alpha)_{nf} = (1-\phi)(\rho\alpha)_f + \phi(\rho\alpha)_{np}$ respectively, where the subscripts l and np refer to the liquid phase of the PCM and the nanoparticles. The changes in density between the liquid and solid phases are neglected.

The energy balance (2) has been written regarding the enthalpy H, with units of energy per volume, and the transport coefficient λ_{eff} represents the effective thermal conductivity. The enthalpy H of the system comes from the contribution of the usual sensible heat, due to changes of temperature in the solid and liquid phases of the pcm and nanoparticles, and from the latent heat content, which is the distinctive feature of PCM materials, i.e.

$$H = H_s + H_l + H_{np} = (1-\phi)(1-f_l)\rho_s\int_{T_{ref}}^{T} c_s(T')dT' + (1-\phi)f_l\rho_l\int_{T_{ref}}^{T} c_l(T')dT' + (1-\phi)f_l\rho_l L + \phi\rho_{np}\int_{T_{ref}}^{T} c_{np}(T')dT' \tag{4}$$

where c_s (ρ_s), c_l (ρ_l), c_{np} (ρ_{np}) are the specific heats (densities) of the PCM in the solid phase, liquid phase, and nanoparticles, respectively. f_l is the volume liquid fraction, and L is the latent heat of the solid/liquid phase change of the PCM. Notice that Eq. (4) provides a consistent thermodynamic formulation to add the effect of nanoparticles on the enthalpy of the system. It can be readily generalized to nonuniform particle distributions and incorporates as well the effect of the nanoparticles on the solid phase of PCM. On supposing constant physical properties in each phase $\rho_l = \rho_S = \rho$, the enthalpy Eq. (2) can be recast in an energy equation in terms of the temperature

$$\left[\frac{\partial}{\partial t} + \mathbf{u}\cdot\nabla\right]\left[\rho(1-\phi)((1-f_l)c_s + f_l c_l) + \rho_{np}\phi c_{np}\right]T = \nabla(\lambda_{eff}\nabla T) - (1-\phi)\rho L\frac{\partial f_l}{\partial t}. \tag{5}$$

When $T_l - T_s$ is a significant fraction of the range of temperature $T_h - T_i$, a relevant consideration in the form of the energy equation comes from the morphology of the solid/liquid interface, called the *mushy region*, as thoroughly discussed in Voller et al. [37] and shown numerically in Voller et al. [38]. At this scenario, the limit case $\mathbf{u}_l = \mathbf{u}_s$ (solid and liquid fully dispersed in the mushy region) corresponds to $\mathbf{u} = \mathbf{u}_l = \mathbf{u}_s$ and leads to the appearance of an advective term for the latent heat in the energy equation; however, the opposed limit case $\mathbf{u}_s = 0$ (solidus fixed and liquid moving around) corresponds to $\mathbf{u} = f_l\mathbf{u}_l$ and there is not such a term. However, for thin mushy regions, like in this work where $(T_l - T_s)/(T_h - T_i) \sim 0.019$ (c.f. Table 1) leads to mushy regions of just hundredths of micrometers, the advective term for the case of solid fully dispersed in the liquid phase is neglectable.

The last term in the momentum equation provides an empirical proportionality relationship, due to Darcy, between the pressure gradient in a porous medium and the fluid velocity within it. The functional form corresponds to the Carman-Kozeny equation and is a convenient way to damp the velocity flow within the mushy region and suppress it at the solid phase. We set in this term the Darcy coefficient $C = 1.6 \cdot 10^6$ kg m^{-3} s, in compliance with previous works [32,1], and $\delta \ll 1$ a tiny constant to avoid division by zero without physical meaning. When the cell is completely liquid ($f_l = 1$) the Darcy term is null, like in a single phase fluid, when it is completely solid ($f_l = 0$) the Darcy term becomes dominant, and the velocity of the liquid becomes null. For intermediate values of f_l ($0 < f_l < 1$), the PCM is in the mushy zone. Through this formulation, the Darcy term allows to use the momentum equation in the whole domain and model the phase change when fluid motion is present without the complication of tracking the solid/liquid interface [35,37].

Finally, the latent heat contained in an elementary volume depends on the liquid fraction as $\Delta H = f_l\rho L_{nf} = f_l\rho(1-\phi)L$. Then the coupling between the energy and momentum equation is given through the liquid fraction f_l, which in turn depends on the temperature, the master variable of the phase change process. The liquid fraction in the mushy zone is modeled by a linear relationship between the solidus and liquidus temperatures

$$f_l = \Delta H/(\rho L_{nf}) = \begin{cases} 0 & \text{if } T \leqslant T_s \\ 1 & \text{if } T \geqslant T_l \\ (T - T_s)/(T_l - T_s) & \text{if } T_s < T < T_l \end{cases} \quad (6)$$

ΔH ranges from 0 (PCM solid) to ρL_{nf} (PCM liquid). The liquid and solid phases coexist for intermediate values.

2.1. Transport coefficients of the nanofluid

2.1.1. Maxwell-Garnett and Brinkmann models

The models more frequently used to predict the thermal conductivity and viscosity of nanoparticles dispersed in liquids are the Maxwell-Garnett and Brinkmann models, respectively. Both are mean field microscopic models, and a large number of works on nanofluids have used these models, from now on M&B (Maxwell and Brinkmann), and are a reference to compare predictions with experimental results.

The Maxwell-Garnett model reads

$$\frac{\lambda_{eff}}{\lambda_l} = \frac{\lambda_{np} + 2\lambda_l - 2\phi(\lambda_l - \lambda_{np})}{\lambda_{np} + 2\lambda_l + \phi(\lambda_l - \lambda_{np})} \quad (7)$$

here λ_{eff}, λ_l and λ_{np} are the effective thermal conductivities of the nanofluid at rest, the liquid phase of the PCM, and nanoparticles, respectively [29]. For particles embedded in solids, like the nanoparticles in the solid phase of the PCM, this is a reliable model and will be used in this work. Notice how it does not depend on the temperature or physical size of the nanoparticles. More complex formulations amend this model adding a term to include contributions to the thermal dispersion due to the Brownian motion. The value of the empirical factor of this coefficient is not stated explicitly in the PCM literature, and other factors like aggregation or fluid/particle molecular interactions make this amended model still lacking to predict effective conductivities [27].

The Brinkmann model for the effective viscosity of the nanofluid treats the nanoparticles as rigid spheres and reads

$$\mu_{eff} = \frac{\mu_f}{(1-\phi)^{2.5}}, \quad (8)$$

where μ_{eff} is the effective viscosity and μ_f the viscosity of the pure fluid [9]. This model is known to underestimate the viscosity of nanofluids when compared with experiments.

2.1.2. Least-Square fit to experimental data

We use an empirical correlation for the effective thermal conductivity and viscosity developed recently by Corcione, from now on LSC (Least-Square Corcione), which exhibits a good agreement with Cu, Al_2O_3, CuO and TiO_2 nanoparticles dispersed in water, ethylene glycol and propylene [12].

There is not a single correlation able to predict the whole array of experimental data, as mentioned in the introduction. However, it is enlightening to compare LSC predictions to experimental data from Ho and Gao [19] on Al_2O_3 dispersed in *n*-octadecane at weight fraction 5%. We obtain for the more sensitive thermal conductivity $k_{eff} = 0.1326$ for $d_{np} = 159.6\,\text{nm}$ at $T = 30\,^\circ\text{C}$, and $k_{eff} = 0.137$ at $T = 60\,^\circ\text{C}$. Both below 10% of discrepancy with respect to the experimental data reported by Ho and Gao. This difference is acceptable taking the perspective that Ho and Gao and another recent set of experimental data by Motahar et al. [30] on pure *n*-octadecane show discrepancies about 10% in the thermal conductivity. The good prediction of LSC is remarkable since it has been developed on metallic nanoparticles dispersed in low molecular weight liquids compared to the high value of paraffins.

The least-square fit to experimental data by Corcione leads to the following prediction for the effective dynamic viscosity

$$\frac{\mu_{eff}}{\mu_l} = \frac{1}{1 - 34.87\left(d_{np}/d_f\right)^{-0.3}\phi^{1.03}} \quad (9)$$

where d_{np} is the nanoparticle diameter, and d_f the equivalent diameter of a pure fluid molecule. This fit does not underestimate the viscosity of nanofluids like Brinkmann's mean field model does. As for the thermal conductivity, the fit is more involved with dependence on the Reynolds number *Re*, Prandtl number *Pr* and temperature according to

$$\frac{\lambda_{eff}}{\lambda_l} = 1 + 4.4\,Re^{0.4}\,Pr^{0.66}\left(\frac{T}{T_l}\right)^{10}\left(\frac{\lambda_{np}}{\lambda_f}\right)^{0.03}\phi^{0.66} \quad (10)$$

More details on these expressions can be found in Corcione [12].

We notice that M&B is a very simplified model for the calculation of transport coefficients on nanofluids. It neglects important physical features like the size of nanoparticles, temperature, and properties of the base fluid. The empirical model LSC brings all these physical parameters into consideration. Although other physical effects are neglected, it narrows the gap between oversimplified and overcomplex models incorporating available experimental quantities.

3. Numerical methods and validation of the model

3.1. Numerical methods

To solve the model presented above, momentum equation modified with a Darcy porous term coupled with an energy equation including a source of latent heat, we use the open source software under GPL license OpenFoam [39]. It is written in C++ making possible a simple top-level description of partial differential equations by operator overloading. Accompanying the basic suite a large collection of tutorials and solvers applicable to a wide range of problems in computational fluid dynamics in the laminar and turbulent regimes are provided. It is designed with parallelization capability for general 3D geometries and can be adapted straightly to 2D and 1D geometries. OpenFoam discretizes partial derivative equations using the Finite Volume Method and has been thoroughly tested and validated during more than a decade in solving mass, energy and momentum conservation equations. The conservation of fluxes insured by the finite volume method makes this discretization specially advantageous when nonlinear advective terms appear as in convection dominated PCM dynamics.

The convective terms are discretized using a second order upwind scheme. The time integration is carried out using a second order Crank-Nicolson scheme. The source term in the energy equation requires particular attention since it couples the temperature and liquid fraction fields strongly. Following Voller and Swaminathan [36], it is linearized as a function depending on temperature, split in an explicit (zero order term) and implicit part (first order term), and the liquid fraction updated at every iteration.

A Rhie-Chow interpolation method is used to solve the enthalpy porosity equations to avoid checkerboard solutions. The momentum and continuity equation are solved using the PIMPLE algorithm, which ensures a right pressure-velocity coupling by combining SIMPLE and PISO algorithms [2]. The temperature equation is solved for each PIMPLE outer-iteration, ensuring the convergence of the velocity, pressure, and temperature fields. To improve convergence under-relaxation factors are used in the velocity, pressure, and temperature with values 0.7, 0.3 and 0.5 respectively.

After the discretization and linearization of the equations, the original PDE problem is transformed in a system of linear equations solved at each iteration using a multi-grid solver with tolerance 10^{-8} for the pressure, velocity and temperature fields, and 10^{-6} for the liquid fraction.

3.2. Validation of the model

We validate the stability and accuracy of the solver with a classical experimental setup [17], finite volume codes of commercial origin [13], in-house [41,32], and based on a finite difference control volume method [8].

A high quality structured hexahedral mesh created with the open-source mesher GMSH is used. The sharp corners between the curved and plane boundaries make the geometry very demanding to secure convergence and special attention has been put to have a fine enough mesh to capture the high velocity and temperature gradients that appear near the boundaries and moving solid/liquid interface.

The dependence of the solution in the grid was tested from coarse to fine grids using 10,000, 30,000, 50,000, 70,000, 90,000, 110,000 and 130,000 cells up to leveling off the residuals of the norm $L_2([0,1])$ of the function f_l^{-1}-to ensure common support for the curves- between consecutive cell sizes. Fig. 2(a) shows the evolution of the overall liquid fraction in *n*-octadecane for the geometry studied in this work at $T_h = 100\,^{\circ}\mathrm{C}$ and initial temperature $T_i = 25\,^{\circ}\mathrm{C}$. Increasing the number of cells reduces the variation of the melting time up to less than 0.5% from 90,000 cells progressively. A grid with this number of cells provides sufficient accuracy for the problems simulated in this work.

The code is as well validated with the benchmark experiment on gallium melting by Gau and Viskanta [17]. In this experiment a narrow parallelepiped enclosure of 63.5 mm height, 88.9 mm length, and 38.1 mm depth is filled with gallium at a uniform internal temperature of 302.95 K. The left hot wall is kept at a constant temperature $T = 311$ K, the right cold at $T = 301.3$ K, and horizontal top and bottom walls are adiabatic. The advance of the solid/liquid interface is shown in Fig. 2(b) at $t = 2, 6, 15$, and 19 min. The quantitative agreement between our simulation and the experiment is reasonable for all the times, capturing the regions of different slopes. Different between simulations and experimental data come from sources like sub-cooling, maintenance of constant temperature at the walls in experiments, or even 3D effects, which have been shown to play a role in the melting of gallium even if the depth of the enclosure is small [7]. Fig. 2(b) shows as well a comparison with the finite difference control volume code of Brent et al. [8]. We obtain a better fit with experimental data at the upper half part of the domain and later melting times, which is probably due to the finer mesh allowed by current processing power. A comparison with Wittig and Nikrityuk [41] shows a more stable front position in our numerical results.

To validate the model and simulations with curved geometries with and without mid-plane symmetry we compare with Darzi et al. [13]. They carry out simulations on melting of *n*-eicoseane between two cylinders of diameter 20 mm and 40 mm in configuration concentric (circles in Fig. 3(a)) and eccentric (squares in 3 (a)) with 5 mm center to center distance. Darzi et al. carried out the simulations with the commercial code Fluent 6.0 using a grid

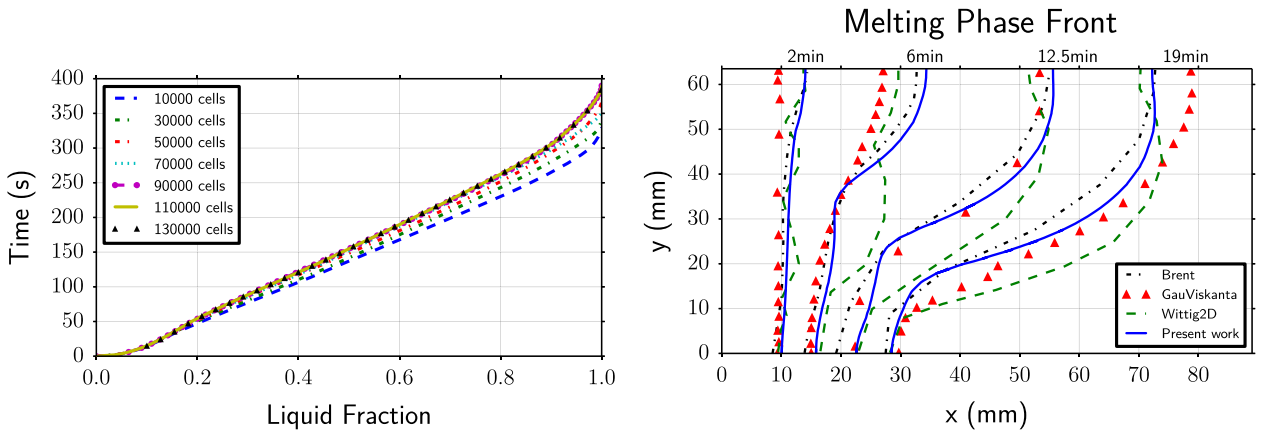

Fig. 2. (a) Evolution of the overall liquid fraction in *n*-octadecane for the geometry of Fig. 1 at $T_h = 100\,^{\circ}\mathrm{C}$ for seven meshes with increasing cell count. (b) Evolution of the solid/liquid interface as a function of time for the benchmark experiment on melting of gallium by Gau and Viskanta [17]. Up triangles correspond to the experimental data, dashed line to simulations by Brent et al. [8], the dash-dotted line to the bidimensional case of Wittig and Nikrityuk [41], and the solid line to our simulations.

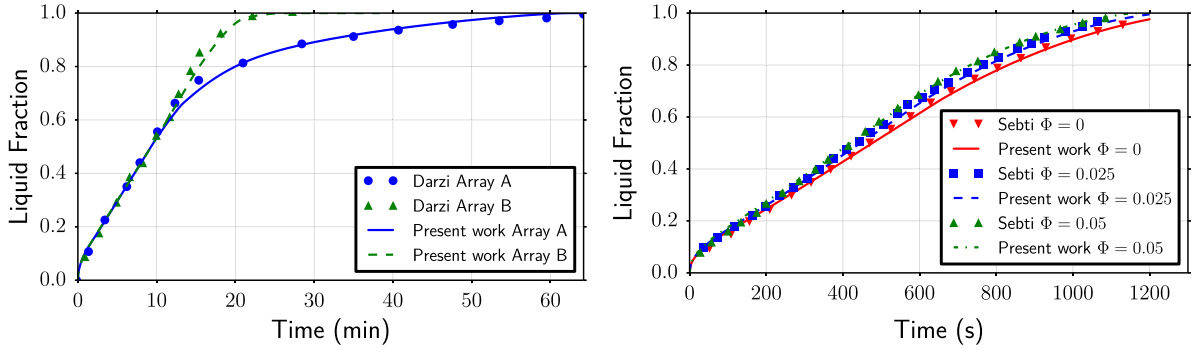

Fig. 3. (a) Evolution of the liquid fraction of *n*-eicosane as a function of time in an annulus. The solid and dashed lines correspond to our results. Circles to Array A of Darzi et al. [13], and triangles to Array B of Darzi et al. [13]. (b) Evolution of the liquid fraction as a function of time in a square enclosure filled with paraffin wax and dispersed copper nanoparticles. Lines correspond to our results and symbols to simulations of Sebti et al. [32]. $\phi = 0$ corresponds to thick line (down triangles), $\phi = 0.025$ to dashed lines (squares), and $\phi = 0.05$ to dash-dot line (up triangles).

of 6470 cells. The agreement between our OpenFoam based model (thick and dashed lines) is good for both geometries, particularly in the linear regime at the beginning of melting and sublinear at the final stages.

Finally, we compare our results with the simulation of a PCM enhanced with metallic nanoparticles carried out by Sebti et al. [32] with an in-house fortran finite volume solver following as well an enthalpy porosity formulation. They used a Brinkman model for viscosity and Maxwell-Garnett for the conductivity. The enclosure is a square cavity of length 10 mm filled with paraffin wax and dispersed copper nanoparticles at volume fractions 0.025 and 0.5. The initial temperature is $T_i = 301.3$ K, the left hot wall is held at $T_c = 306.3$ K and the rest of walls are adiabatic. Our results showed in Fig. 3(b) superpose to Sebti et al., indicating an excellent fit during the whole melting process at all volume fractions. Notice that simulations have been validated from paraffin waxes, which exhibit a slow conductive and convective transport, to the liquid metal gallium with very high heat transport rate.

4. Results and discussion

The addition of metallic nanoparticles increases the effective thermal conductivity and viscosity of the base fluid in convection. These two effects are competitive as for the final heat transfer capability of the nanofluid. If the first is dominant a faster melting of the PCM will be promoted with nanoparticles, if the second is dominant then a slower melting is expected. The relative strength of both effects can be evaluated using the effective Prandtl number $Pr_{eff} = \nu_{eff}/\kappa_{eff}$, where ν_{eff} is the effective kinematic viscosity and κ_{eff} the effective thermal diffusivity.

Features of the nanofluid, such as small nanoparticle concentration, small particle diameter or high temperature promote the underestimation of conductivity by Maxwell-Garnett with respect to LSC. Opposite features favor the inverse situation. On the other hand, Brinkman's model underestimates the viscosity for all nanoparticle sizes, temperatures, and nanoparticle concentrations with respect to LSC, being this effect more pronounced for small particles. Thus LSC predicts a lower effective Prandtl number (and increased heat transfer rate) than M&B for very small nanoparticles at high temperatures and low concentrations. For the rest of the cases, M&B predicts a lower effective Prandtl number. This behavior is illustrated in Fig. 4 for selected temperatures and nanoparticle sizes of Al_2O_3 dispersed in *n*-octadecane. M&B shows a monotonic decrease of Pr_{eff} with the volume fraction, thus predicting a continuous improvement of the heat transfer rate of the nanofluid with increasing ϕ. However, LSC shows a monotonic increase of Pr_{eff} from either $\phi = 0$ or a local minimum at low concentrations below *Pr* of the base fluid. In light of this only enhanced heat transfer, at fixed temperature, is expected within a narrow range of ϕ. In short, from Fig. 4 one expects faster melting time using M&B at most of the nanoparticle concentrations compared to LSC, leading to an overestimation of the heat transfer performance in PCMs with nanoparticles compared to that predicted by an empirical fit of the transport coefficients.

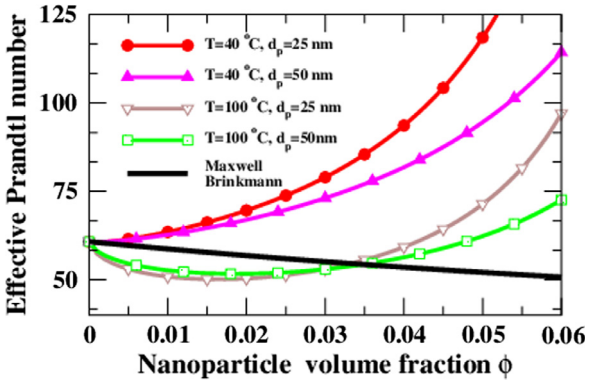

Fig. 4. Effective Prandtl number as a function of the nanoparticle volume fraction ϕ predicted by Corcione's least-square empirical fit (symbols) and Maxwell&Brinkmann (solid line) models.

4.1. Conductive transport

A reference to the overall effect of natural convection in the dynamics of PCM melting is provided taking into account first only transport by conduction, i.e. using only Eq. (5). Evolution of the overall liquid fraction as a function of time is shown in Fig. 5, where the conductive hot curved wall is held at $T_h = 100\,^{\circ}$C and an initial temperature of 25 °C is used. Inclusion of nanoparticles modifies the conductivity of the solid and stagnant melted part, but there is not particle diffusion and a Maxwell-Garnett model is suitable to calculate the effective thermal conductivity. The melting time for the base fluid is 3442 s, nanoparticles at a volume fraction $\phi = 0.01$ reduce it about 3.9% to 3308 s, 19.4% for $\phi = 0.06$, and 32.2% for $\phi = 0.11$. This improved heat storage rate is expected due to the much higher conductivity of the metallic nanoparticles.

The lower conductivity of the liquid phase with respect to the solid phase leads to a quick advance of the overall liquid fraction in the first states of melting, requiring about 85% of the melting time to melt the last 50% of the PCM where the liquid phase is dominant. The slowing down of the melting rate is observed as a loss of linearity of the overall liquid fraction curve at $f_l = 0.5$, where a sub-linear regime appears at a log-log scale. This reduction of the melting time under conduction has been observed as well in experiments of Cu nanoparticles in paraffin, although physical properties of the used paraffin are not provided [43]. At larger particle concentrations $\phi = 0.06$ and 0.11 we observe a similar advance of the overall liquid fraction, scaling with $f_l(t) \sim t^{0.47}$, and a faster decay in the final sub-linear regime.

4.2. Convective transport

We present in this section the results including as well the convective motion driven by buoyancy. The impact on the heat transfer process of the nanofluid is huge since overall the convective motion decrease the melting time by a factor ten. Not surprisingly,

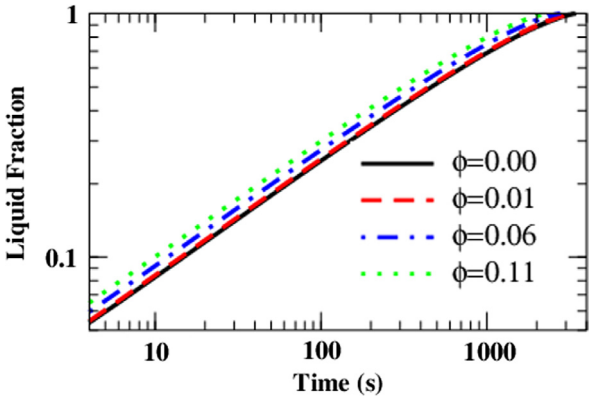

Fig. 5. Evolution of the liquid fraction as a function of time in log-log scale for *n*-octadecane when only conductive heat transport is considered. Effective conductivity of the phases solid and quiescent liquid are calculated using the Maxwell-Garnett model. Conductive curved boundary is held at $T_h = 100\,^{\circ}$C. (i) (thick line) $\phi = 0.0$, (ii) (dashed line) $\phi = 0.01$, (iii) (dot-dashed line) $\phi = 0.06$, (iv) (dotted line) $\phi = 0.11$

favoring convective motion is frequently used to reduce the heat storage and release times in applications of PCMs.

We can calculate an effective Rayleigh number during the melting in the region below the solidus $Ra_{eff} = g\,\alpha\,\Delta T h^3/(\kappa_{eff}\,\nu_{eff})$, where $\Delta T = T_h - T_i$ and h is the thickness between the boundary at the lowest part of the domain and the solidus along the vertical symmetry axis. A maximum Ra_{eff} can be estimated when h reaches the half of the depth along the vertical symmetry axis. Thus for pure n-octadecane Ra extends up to $1.9 \cdot 10^6$. Increasing ϕ, M&B shrinks slightly the range up to $Ra_{eff} \sim 1.8$ for $\phi = 0.06$, and LSC more strongly to $Ra_{eff} = 3.3 \cdot 10^5$ for $\phi = 0.06$.

The two main regimes observed in the overall liquid fraction curve can be derived from the classic Rayleigh-Bénard theory of convection in a horizontal liquid layer heated from below. When h is small Ra_{eff} is small and the viscous and thermal dissipation stronger than the destabilizing buoyancy and heat transport takes place by conduction. This first conductive regime appears as an initial linear growth of the Rayleigh number as a function of time in the log-log scale of Fig. 6 (up to ~40 s at $\phi = 0$). As the solid/liquid interface advances Ra_{eff} increases and the buoyancy force becomes dominant, leading to the destabilization of the quiescent liquid at the bottom of the disk and the appearance of a layer of convective cells. As a reference, for a horizontal layer of n-octadecane bounded by rigid plates, the destabilization takes places when Ra reaches the critical value 1708 at a thickness of 1.5 mm. This second convection dominated regime is faster, starts at the end of the first linear growth stage of Fig. 6 (from ~40 s at $\phi = 0$), and leads to an almost linear growth of the overall liquid fraction curve up to the latest phase of PCM melting at ~85% of the overall liquid fraction. There the strong shrinkage of the more conductive solid phase declines the slope of the overall liquid fraction curve (c.f. Figs. 7 and 8). Within the convection dominated regime, there are additional sub-regimes that depend on specifics physical parameters.

The other primary mechanism behind the dynamics of melting is the lateral heating dominant nearby the upper free surface due to the symmetry of the disk heated from the curved boundary. Interestingly, from the zone between lateral and vertical dominant cold plumes emerge from the colder solid side and may lead to strong temperature gradients near the conductive wall. Lateral heating leads quickly to the formation of a single large convective cell with liquid moving upwards adjacent to the conductive wall, roughly parallel to the free surface and falling near the colder solid/liquid interface. Since fluid velocity is stronger near the upper flat surface there is a more substantial advance of the solid/liquid interface at this region that breaks the circular symmetry of the solidus (c.f. Figs. 9 and 11).

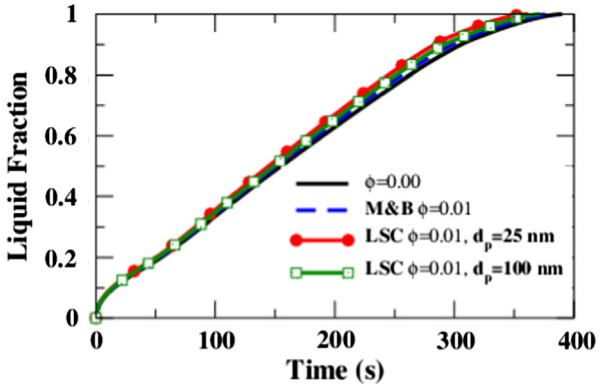

Fig. 7. Evolution of the liquid fraction of n-octadecane for $T_h = 100\,^{\circ}$C. (i) (solid line) base fluid, (ii) (dashed line) M&B model with $\phi = 0.01$, (iii) LSC model with $\phi = 0.01$ for $d_{np} = 25$ nm (circles) and $d_{np} = 100$ nm (squares).

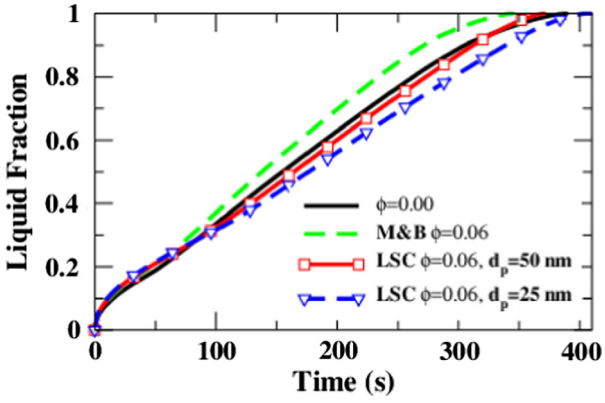

Fig. 8. Evolution of the liquid fraction of n-octadecane for $T_h = 100\,^{\circ}$C. (i) (solid line) base fluid, (ii) (dashed line) M&B model with $\phi = 0.06$, (iii) (squares) LSC model for $\phi = 0.06$ and $d_{np} = 50$ nm, (iv) (triangles down) LSC model for $\phi = 0.06$ and $d_{np} = 25$ nm.

4.2.1. Volume fraction $\phi = 0.01$

We first carry out simulations in the region where M&B predicts larger Pr_{eff} than LSC. Fig. 7 exhibits the evolution of the overall liquid fraction of n-octadecane during melting with $T_h = 100\,^{\circ}$C. M&B provides a single curve, independent of the nanoparticle size. As expected, the melting time is the longest in the absence of metallic nanoparticles (390 s). The inclusion of Al_2O_3 nanoparticles at $\phi = 0.01$ leads to a small decrease of the melting time using

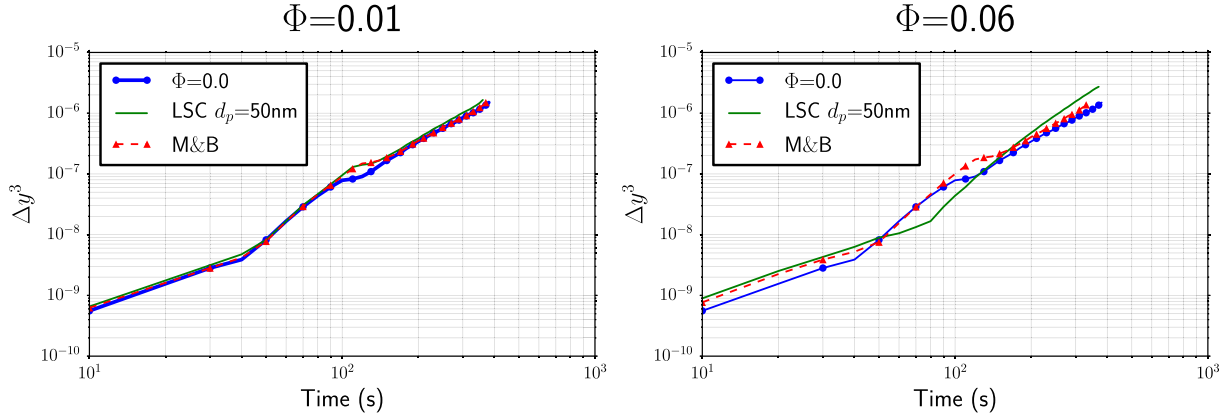

Fig. 6. Δy^3 (space dependence of the Rayleigh number) as a function of the time measured across the vertical axis of symmetry of the semicircle. The solid line corresponds to LSC for $d_{np} = 50$ nm, and the dashed-lines with symbols to M&B.

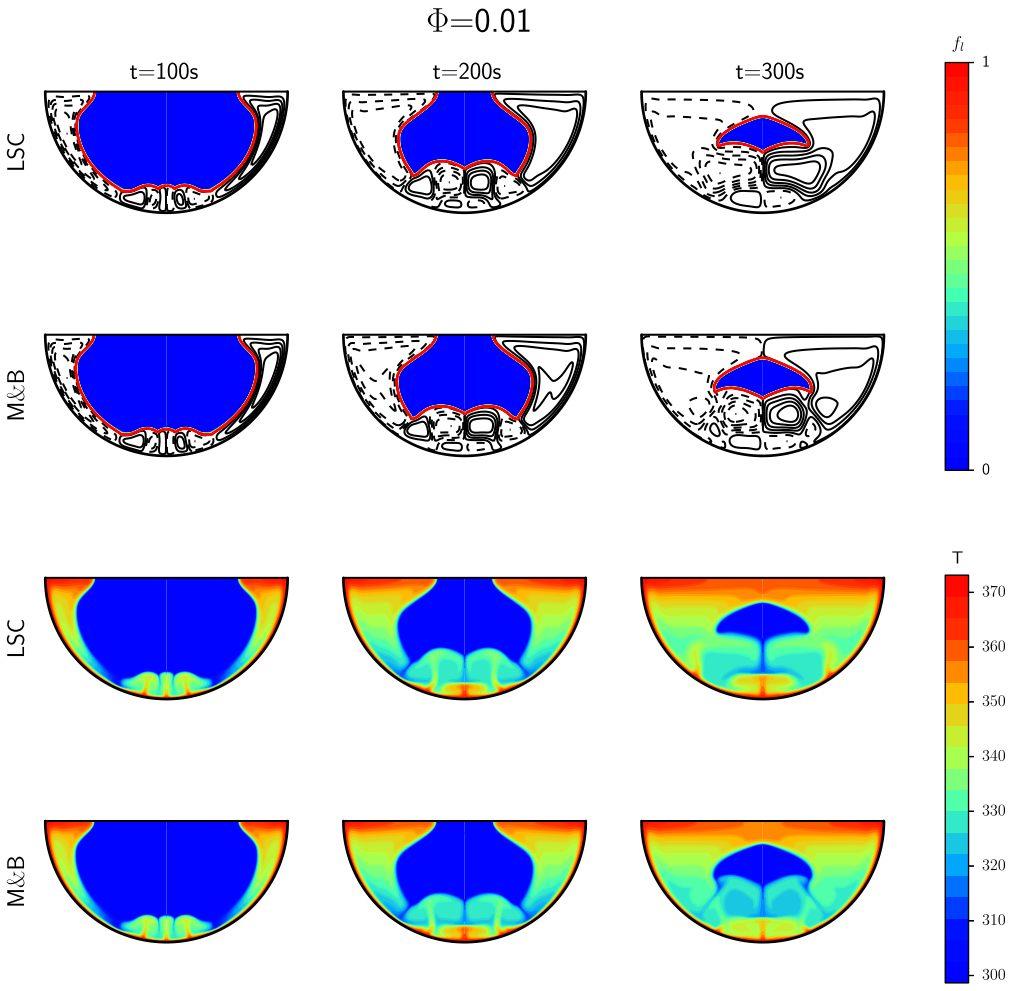

Fig. 9. Snapshots at $t = 100$ s, 200 s and 300 s of the temperature field (third and fourth rows) and streamlines (first and second rows) for volume fraction $\phi = 0.01$. First and third rows exhibit the results for the transport coefficients calculated according to LSC for $d_{np} = 50$ nm, and second and fourth to M&B.

M&B (380 s). Instead, if the empirical LSC is used to calculate the transport coefficients, we find a larger reduction of the melting time: 372 s, 368 s and 360 s for particles diameters of 100 nm, 50 nm, and 25 nm nanometers, respectively. For the smallest particles, $d_{np} = 25$ nm, LSC leads to a melting time reduction of 5.6% with respect to M&B.

A sequence of snapshots for streamlines and temperature fields at $t = 100, 200$ and 300 s for M&B and LSC is shown at Fig. 9. At $t = 100$ s three pairs of counter-rotating convective cells are generated at the bottom of the disk after a Rayleigh-Bénard instability at the onset of convection. The snapshots of the temperature field show a hot plume wherever a pair of counter-rotating cells moves upwards. This hotter ascending liquid leads to a deeper advance of the solid/liquid interface at these regions generating three concave parts at the bottom of the solidus boundary.

As melting continues at $t = 200$ s the dynamics of the LSC and M&B is qualitatively the same. The increased gap of the melted part at the bottom gives room to the creation of two superposed layers of convective cells. This happens through the shift of the outer pairs of cells at 100 s and their superposition over the central pair. All that is accompanied by an increase in the size of all cells and is observed as well in the temperature field, where the central plume becomes caught between the ones outside. The superposition of the convective cells is as well observed in Fig. 6 from ∼110 s to ∼ 40 s with a slowdown of the speed of propagation of the solid/liquid front.

At $t = 300$ s different dynamics between M&B and LSC begins to appear. LSC shows a reconnection of the upper layer of cells merging as well with the large lateral cell, leaving just a single pair of small cells at the bottom split from the general circulation. The large laterally dominated flow of the upper part leads to a plume of cold fluid descending through the symmetry axis of the domain up to touching the hot plume rising from the bottom. Meanwhile, M&B shows a state where reconnection of cells has not happened. This makes M&B more inefficient in the heat transport with respect to LSC where large convective cells carry the heat from the hot wall to the colder solidus. The effect of this process is the reduced size of the solidus in the LSC model compared to M&B.

Interestingly, the overall dynamics of the melting process can be tracked from the motion of cold and hot plumes which can be located through the local Nusselt number, defined as the local dimensionless heat flux:

$$Nu(\theta) = \frac{R}{\kappa_f \Delta T} \kappa_{eff}(\theta) \mathbf{n} \cdot \nabla T. \tag{11}$$

where R is the semicircle radius, ΔT is the difference between the melting temperature and T_h, κ_f is the n-octadecane thermal conductivity, κ_{eff} is the effective thermal conductivity at the wall, and $\mathbf{n}$ is the outward unit vector normal to the boundary. Fig. 10 exhibits the variation of the local Nusselt number at the conductive boundary as a function of the angle in polar coordinates. At

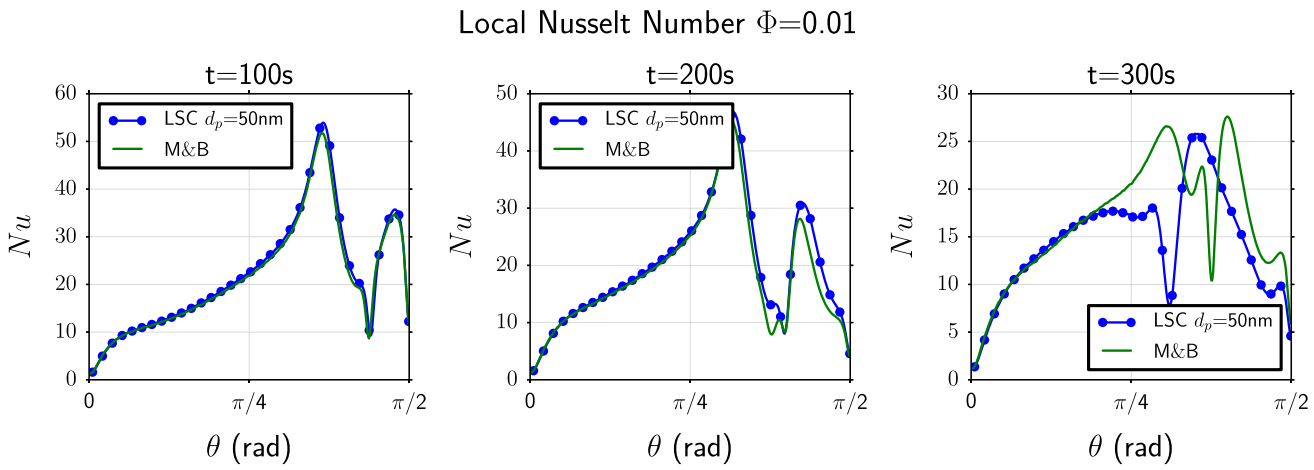

Fig. 10. Local Nusselt number at $\phi = 0.01$ for $t = 100$ s, 200 s and 300 s calculated at the curved boundary of the domain as a function of the angle in polar coordinates. Solid line corresponds to M&B, line with symbols (circles) to LSC for $d_{np} = 50$ nm.

$t = 100$ s there is an absolute maximum at $\theta \sim 3\pi/8$ and a local minimum closer to the vertical axis. The position of the maximum corresponds to plumes of cold liquid approaching the hot wall, and minimum corresponds to hot plumes emerging from the wall (c.f. third and fourth rows of Fig. 9). At $t = 200$ s the maximum and minimum shift towards lower angles, but overall curve is the same. However, at latest times $t = 300$ s local Nusselt curves for M&B and LSC begin to separate as expected from the very different temperature field of Fig. 9.

4.2.2. Volume fraction $\phi = 0.06$

Prandtl number for base *n*-octadecane is 60.8 according to Fig. 4. M&B predicts a decline to $Pr_{eff} = 50.8$ for $\phi = 0.06$. However, at this volume fraction LSC predicts a surge to $Pr_{eff} = 72.6$ for $d_{np} = 50$ nm, and $Pr_{eff} = 97$ for $d_{np} = 25$ nm. Thus a decrease in the heat transfer rate is expected for the latter model. This is confirmed in Fig. 8, where the liquid fraction for M&B is above LSC once convection sets in. Furthermore, the melting time for M&B is $345.1s$, while for LSC is $371.4s$ ($d_{np} = 50$ nm) and $406s$ ($d_{np} = 25$ nm). This scenario where effective Prandtl number is lower for M&B than LSC is the most frequent situation in simulations and experiments, and that leads to an overestimation of the melting rate of M&B, as shown in the liquid fraction curves.

A sequence of snapshots at $t = 100, 200$ and 300 s for streamlines and temperature fields for M&B and LSC is displayed at Fig. 11. At $t = 100$ s only a pair of well formed counter-rotating convective

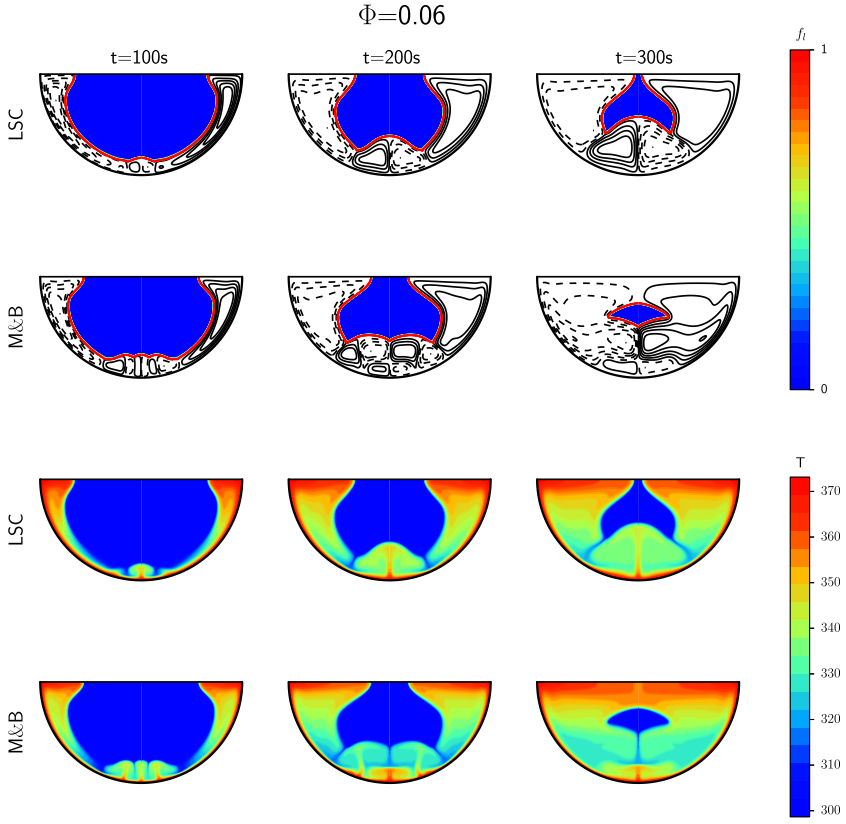

Fig. 11. Snapshots at $t = 100$ s, 200 s and 300 s of the temperature field (third and fourth rows) and streamlines (first and second rows) for volume fraction $\phi = 0.06$. First and third rows exhibit the results for the transport coefficients calculated according to LSC for $d_{np} = 50$ nm, and second and fourth for M&B.

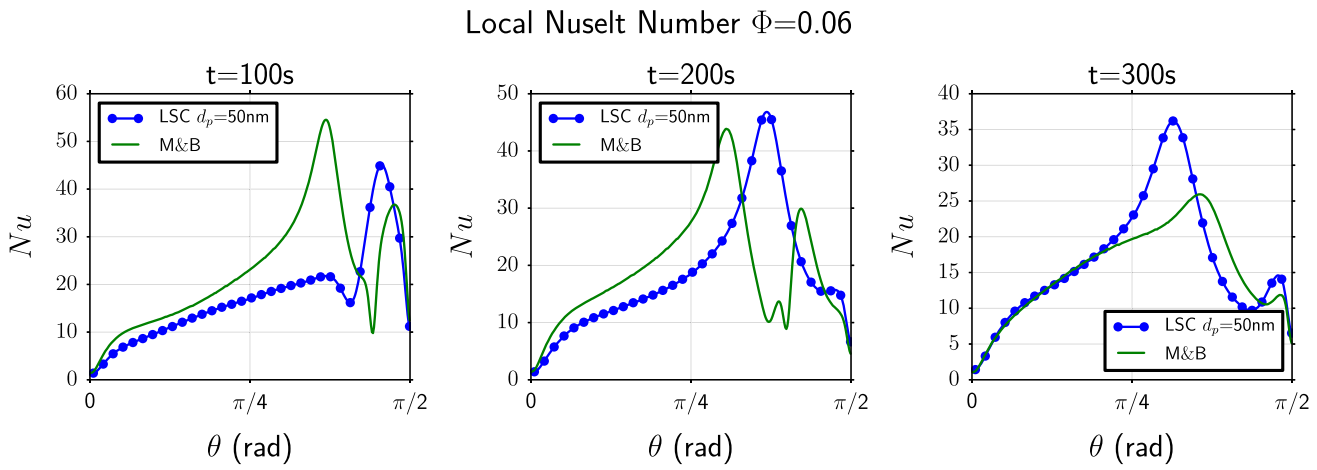

Fig. 12. Local Nusselt number at $\phi = 0.06$ for $t = 100$ s, 200 s and 300 s calculated at the curved boundary of the domain as a function of the angle in polar coordinates. Solid line corresponds to M&B, line with symbols (circles) to LSC for $d_{np} = 50$ nm.

cells are generated at the bottom of the domain for LSC, meanwhile, for M&B we have three pairs of convective cells (and three ascending hot plumes) and more advanced solid/liquid interface, showing the enhanced heat transfer rate predicted by M&B for $\phi = 0.06$, and decreased for LSC with respect to $\phi = 0.01$.

At further times 200 and 300 s, LSC overall circulation continues to be the same, with a single hot plume arising at the bottom. However, M&B simulations evolve as LSC at $\phi = 0.01$, with cold and hot plumes touching in the symmetry axis. This reflects the close Pr_{eff} exhibited in both cases. Comparing solidus of both of LSC and M&B models for $\phi = 0.06$ at 300 s shows a minor area of solidus left for M&B.

As in case $\phi = 0.01$, the overall dynamics of the melting process with $\phi = 0.06$ can be tracked from the motion of cold and hot plumes using the local Nusselt number. In the latest case, the local Nusselt curves (Fig. 12) for M&B and LSC differ for all shown times because of the different configuration of convective cells resulting from M&B and LSC model.

Fig. 4 shows that final melting time of the PCM depends on the interplay between conductive and convective processes. The melting time with LSC for $\phi = 0.06$ and $d_{np} = 50$ nm is slightly shorter than without nanoparticles in spite of the increased effective Prandtl number for LSC. The first factor explaining this behavior is the enhanced conductivity of the solid phase by the presence of metallic nanoparticles leading to a faster heat transfer rate while the conduction dominates the melting process, up to $f_l \sim 0.2$ in Fig. 8. In this regime, the overall liquid fraction curve of the base fluid is below the cases with nanoparticles. The second factor deals with the configuration of convective cells and plumes at the latter stages of melting, which determines the evolution of the very small fraction of solidus area at this stage. The LSC model exhibits two convective cells at the bottom, one on each side of the symmetry axis generating a reduced viscous dissipation compared to more involved configurations, and a hot plume in the symmetry axis enhancing the heat transfer in the zones nearby. This improvement in the heat transfer along the symmetry axis is seen as well in Fig. 6 (b), where the lack of the transition regime of superimposed cells for LSC with $\phi = 0.06$ accelerates the motion of the solid/liquid front.

This analysis illustrates that while the effective Prandtl number has the strongest influence in the melting process (as observed in LSC for $d_{np} = 25$ nm during the whole melting), one must take into account more factors to explain the melting dynamics; such as the duration and extension of conductive dominated regime, or the state at the latter phase of melting.

5. Conclusions

We have carried out a numerical study on melting dynamics of the PCM *n*-octadecane with Al_2O_3 nanoparticles uniformly dispersed at small concentrations. A semicircular geometry of radius 2 cm has been selected, whose curved part is held at constant temperature and free surface is adiabatic. The phase change problem, with the complication of a moving solid/liquid interface, has been modeled using an enthalpy-porosity formulation. The numerical procedure is based on finite volumes using the Open Source software OpenFoam.

The effect of metallic nanoparticles on the solid phase of the PCM has been modeled via a Maxwell-Garnett relation for the conductivity. The enhanced conductivity of the solid phase due to the metallic nanoparticles has been shown to be important in the reduction of the overall melting time of the PCM. The modeling of the effective conductivity and viscosity of the liquid phase of the PCM has been carried out through mean field models, Maxwell-Garnett for conductivity and Brinkmann for viscosity, and an empirical model based on a fit to experimental data proposed by Corcione. Predictions of both models are compared in the article. Nanoparticles of small size, high temperature and small volume fractions favor a lower effective Prandtl number -and enhanced rate of melting- for Corcione's, the opposite situation promotes a lower effective Prandtl number for M&B. The most frequent cases studied numerically in the literature are found within the favorable M&B regime, which leads to an overestimation of the reduction of melting times for the convective regime compared with the empirical model due to Corcione. However, we have shown that is possible to choose the size of alumina nanoparticles, volume fractions, and temperatures where the NePCM exhibits an improved heat transfer rate with respect to what is predicted by the simpler M&B model. In these situations, NePCM become even more attractive for thermal management and energy storage applications.

Our results agree with experiments carried out by Ho and Gao in *n*-octadecane with dispersed Al_2O_3 nanoparticles, where no improvement of the heat transfer rate in the convective regime was forecasted based upon measures of effective conductivity and viscosity.

There exists no universal fit to experimental data of the effective conductivity and viscosity and LSC is more likely not the best possible option. However, our results show that predictions of heat transfer rates of nanofluid based PCMs with classic mean field models like M&B are generally overestimated, and a careful

combination of fluid and nanoparticles must be selected to improve the heat transfer rate.

Acknowledgements

Santiago Madruga acknowledges support by Erasmus Mundus EASED programme (Grant 2012-5538/004-001) coordinated by Centrale Supélec, the Spanish *Ministerio de Economía y Competitividad* under Projects No. TRA2016-75075-R, No. ESP2013-45432-P and No. ESP2015-70458-P, and the computer resources and technical assistance provided by the Centro de Supercomputación y Visualización de Madrid (CeSViMa).

References

[1] M. Abdollahzadeh, M. Esmaeilpour, Enhancement of phase change material (PCM) based latent heat storage system with nano fluid and wavy surface, Int. J. Heat Mass Transfer 80 (2015) 376–385.
[2] H.J. Aguerre, S. Marquez Damian, J.M. Gimenez, N.M. Nigro, Modeling of compressible fluid problems with openfoam using dynamic mesh technology, Mecánica Comput. XXXII (2013) 995–1011.
[3] F. Agyenim, P. Eames, M. Smyth, A comparison of heat transfer enhancement in a medium temperature thermal energy storage heat exchanger using fins, Sol. Energy 83 (9) (2009) 1509–1520.
[4] E.M. Alawadhi, Thermal analysis of a building brick containing phase change material, Energy Build. 40 (3) (2008) 351–357.
[5] A.V. Arasu, A.S. Mujumdar, Numerical study on melting of paraffin wax with Al_2O_3 in a square enclosure, Int. Commun. Heat Mass Transfer 39 (1) (2012) 8–16.
[6] E. Assis, G. Ziskind, R. Letan, Numerical and experimental study of solidification in a spherical shell, J. Heat Transfer 131 (2) (2009) 024502.
[7] O. Ben-David, A. Levy, B. Mikhailovich, A. Azulay, 3D numerical and experimental study of gallium melting in a rectangular container, Int. J. Heat Mass Transfer 67 (2013) 260–271.
[8] A. Brent, V. Voller, K. Reid, Enthalpy-porosity technique for modelling convection-diffusion phase change: application to the melting of a pure metal, Numer. Heat Transfer 13 (1988) 297–318.
[9] H.C. Brinkman, The viscosity of concentrated suspensions and solutions, J. Chem. Phys. 20 (1952), pp. 571–571.
[10] J. Buongiorno, D.C. Venerus, N. Prabhat, T. McKrell, J. Townsend, R. Christianson, Y.V. Tolmachev, P. Keblinski, L.W. Hu, J.L. Alvarado, I.C. Bang, S. W. Bishnoi, M. Bonetti, F. Botz, A. Cecere, Y. Chang, G. Chen, H. Chen, S.J. Chung, M.K. Chyu, S.K. Das, R. Di Paola, Y. Ding, F. Dubois, G. Dzido, J. Eapen, W. Escher, D. Funfschilling, Q. Galand, J. Gao, P.E. Gharagozloo, K.E. Goodson, J.G. Gutierrez, H. Hong, M. Horton, K.S. Hwang, C.S. Iorio, S.P. Jang, A.B. Jarzebski, Y. Jiang, L. Jin, S. Kabelac, A. Kamath, M.A. Kedzierski, L.G. Kieng, C. Kim, J.H. Kim, S. Kim, S.H. Lee, K.C. Leong, I. Manna, B. Michel, R. Ni, H.E. Patel, J. Philip, D. Poulikakos, C. Reynaud, R. Savino, P.K. Singh, P. Song, T. Sundararajan, E. Timofeeva, T. Tritcak, A.N. Turanov, S. Van Vaerenbergh, D. Wen, S. Witharana, C. Yang, W.H. Yeh, X.Z. Zhao, S.Q. Zhou, A benchmark study on the thermal conductivity of nanofluids, J. Appl. Phys. 106 (9) (2009).
[11] J. Caldwell, C.-c. Chan, Spherical solidi ® cation by the enthalpy method and the heat balance integral method, Appl. Math. Model. 24 (2000) 45–53.
[12] M. Corcione, Empirical correlating equations for predicting the effective thermal conductivity and dynamic viscosity of nanofluids, Energy Convers. Manage. 52 (1) (2011) 789–793.
[13] A.R. Darzi, M. Farhadi, K. Sedighi, Numerical study of melting inside concentric and eccentric horizontal annulus, Appl. Math. Model. 36 (9) (2012) 4080–4086.
[14] N.S. Dhaidan, J.M. Khodadadi, T.A. Al-Hattab, S.M. Al-Mashat, Experimental and numerical investigation of melting of NePCM inside an annular container under a constant heat flux including the effect of eccentricity, Int. J. Heat Mass Transfer 67 (2013) 455–468.
[15] N.S. Dhaidan, J.M. Khodadadi, T.a. Al-Hattab, S.M. Al-Mashat, Experimental and numerical investigation of melting of phase change material/nanoparticle suspensions in a square container subjected to a constant heat flux, Int. J. Heat Mass Transfer 66 (2013) 672–683.
[16] N.S. Dhaidan, J.M. Khodadadi, T.a. Al-Hattab, S.M. Al-Mashat, Experimental and numerical study of constrained melting of *n*-octadecane with CuO nanoparticle dispersions in a horizontal cylindrical capsule subjected to a constant heat flux, Int. J. Heat Mass Transfer 67 (2013) 523–534.
[17] C. Gau, R. Viskanta, Melting and solidification of a pure metal on a verticall wall, J. Heat Transfer. 108 (1) (1986) 174–181.
[18] L. Godson, B. Raja, D. Mohan Lal, S. Wongwises, Enhancement of heat transfer using nanofluids-an overview, Renew. Sustain. Energy Rev. 14 (2) (2010) 629–641.
[19] C.J. Ho, J.Y. Gao, Preparation and thermophysical properties of nanoparticle-in-paraffin emulsion as phase change material, Int. Commun. Heat Mass Transfer 36 (5) (2009) 467–470.
[20] S.F. Hosseinizadeh, A.A.R. Darzi, F.L. Tan, Numerical investigations of unconstrained melting of nano-enhanced phase change material (NEPCM) inside a spherical container, Int. J. Therm. Sci. 51 (1) (2012) 77–83.
[21] S.F. Hosseinizadeh, A.A. Rabienataj Darzi, F.L. Tan, J.M. Khodadadi, Unconstrained melting inside a sphere, Int. J. Therm. Sci. 63 (2013) 55–64.
[22] S. Jegadheeswaran, S.D. Pohekar, Performance enhancement in latent heat thermal storage system: a review, Renew. Sustain. Energy Rev. 13 (9) (2009) 2225–2244.
[23] S. Jesumathy, M. Udayakumar, S. Suresh, Experimental study of enhanced heat transfer by addition of CuO nanoparticle, Heat Mass Transfer 48 (6) (2012) 965–978.
[24] S. Kashani, A.A. Ranjbar, M.M. Madani, M. Mastiani, H. Jalaly, Numerical study of solidification of a nano-enhanced phase change material (NEPCM) in a thermal storage system, J. Appl. Mech. Tech. Phys. 54 (5) (2013) 702–712.
[25] J.M. Khodadadi, S.F. Hosseinizadeh, Nanoparticle-enhanced phase change materials (NEPCM) with great potential for improved thermal energy storage, Int. Commun. Heat Mass Transfer 34 (5) (2007) 534–543.
[26] J.M. Khodadadi, Y. Zhang, Effects of buoyancy-driven convection on melting within spherical containers, Int. J. Heat Mass Transfer 44 (8) (2001) 1605–1618.
[27] C. Kleinstreuer, Y. Feng, Experimental and theoretical studies of nanofluid thermal conductivity enhancement: a review, Nanoscale Res. Lett. 6 (1) (2011) 439.
[28] K.C. Lin, A. Violi, Natural convection heat transfer of nanofluids in a vertical cavity: Effects of non-uniform particle diameter and temperature on thermal conductivity, Int. J. Heat Fluid Flow 31 (2) (2010) 236–245.
[29] J. Maxwell, A Treatise on Electricity and Magnetism, third ed., Dover Publications, 1954.
[30] S. Motahar, N. Nikkam, A.A. Alemrajabi, R. Khodabandeh, M.S. Toprak, M. Muhammed, A novel phase change material containing mesoporous silica nanoparticles for thermal storage: a study on thermal conductivity and viscosity, Int. Commun. Heat Mass Transfer 56 (2014) 114–120.
[31] M. Nourani, N. Hamdami, J. Keramat, A. Moheb, M. Shahedi, Thermal behavior of paraffin-nano-Al_2O_3 stabilized by sodium stearoyl lactylate as a stable phase change material with high thermal conductivity, Renew. Energy 88 (2016) 474–482.
[32] S.S. Sebti, M. Mastiani, H. Mirzaei, A. Dadvand, S. Kashani, S.A. Hosseini, Numerical study of the melting of nano-enhanced phase change material in a square cavity, J. Zhejiang Univ. Sci. A 14 (5) (2013) 307–316.
[33] L. Solomon, A.F. Elmozughi, A. Oztekin, S. Neti, Effect of internal void placement on the heat transfer performance Encapsulated phase change material for energy storage, Renew. Energy 78 (2015) 438–447.
[34] F.L. Tan, S.F. Hosseinizadeh, J.M. Khodadadi, L. Fan, Experimental and computational study of constrained melting of phase change materials (PCM) inside a spherical capsule, Int. J. Heat Mass Transfer 52 (15–16) (2009) 3464–3472.
[35] V. Voller, C. Prakash, A fixed grid numerical modelling methodology for convection-diffusion mushy region phase-change problems, Int. J. Heat Mass Transfer 30 (8) (1987) 1709–1719.
[36] V. Voller, C. Swaminathan, General source–based method for solidification phase change, Numer. Heat Transfer Part B 19 (1991) 175–189.
[37] V.R. Voller, A.D. Brent, C. Prakash, The modelling of heat, mass and solute transport in solidification systems, Int. J. Heat Mass Transfer 32 (9) (1989) 1719–1731.
[38] V.R. Voller, A.D. Brent, C. Prakash, Modelling the mushy region in a binary alloy, Appl. Math. Model. 14 (6) (1990) 320–326.
[39] H.G. Weller, G. Tabor, A tensorial approach to computational continuum mechanics using object-oriented techniques, Comput. Phys. 12 (6) (1998) 620–631.
[40] D. Wen, G. Lin, S. Vafaei, K. Zhang, Review of nanofluids for heat transfer applications, Particuology 7 (2) (2009) 141–150.
[41] K. Wittig, P.a. Nikrityuk, Three-dimensionality of fluid flow in the benchmark experiment for a pure metal melting on a vertical wall, IOP Conf. Ser. Mater. Sci. Eng. 27 (2012) 012054.
[42] S. Wu, D. Zhu, X. Li, H. Li, J. Lei, Thermal energy storage behavior of Al_2O_3-H_2O nanofluids, Thermochim. Acta 483 (1-2) (2009) 73–77.
[43] S.Y. Wu, H. Wang, S. Xiao, D.S. Zhu, An investigation of melting/freezing characteristics of nanoparticle-enhanced phase change materials, J. Therm. Anal. Calorim. 110 (3) (2012) 1127–1131.